13 Phase transitions and superconducting photon detectors

A. Aeschbacher, F. von Rohr, H. Grundmann, O. Bossen, K. Inderbitzin, H. Bartolf, M. Reibelt, S. Siegrist, A. Engel and A. Schilling

in collaboration with: University of Bern (K. Krämer), Tohoku University (N. Toyota), Karlsruhe Institut für Technologie (K. Il'in), Deutsches Zentrum für Luft- und Raumfahrt (H.-W. Hübers, A. Semenov), FIRST Lab ETH Zürich, ESRF Grenoble (C. Mazzoli), PSI Villigen (M. Medarde).

13.1 Physics of superconducting thin-film nanostructures and fast single-photon detectors

Within our project on superconducting nanowire single-photon detectors (SNPD, for a description of the detectors and their detection mechanism, see one of the previous reports), we have mainly followed two directions in the past year.

One objective has been to explore alternatives to the NbN thin films that are almost exclusively used for such detectors. A good detector material for SNPD has to fulfill several requirements. An absorbed photon has to generate a large quantity of quasi-particles, *i.e.* broken Cooper-pairs, favoring materials with small superconducting energy gap. The quasi-particles should be concentrated around the absorption site, thus their diffusion coefficient D must be small. And last but not least, the minimum volume needed to become normal-conducting in order to generate a detectable voltage signal should be as small as possible, leading to the requirement of a short coherence length ξ for the dimension in the applied-current direction and a small cross-sectional area of the superconducting strip, *i.e.* ultra-thin films ($\sim$ nanometer) and the applicability of state-of-the-art nanostructuring techniques to achieve strip widths of 100 nm or less.

Although NbN does fulfill all of these requirements it has certain limitations. Besides difficulties in fabricating high-quality thin films—which can in principle be overcome—NbN has a relatively high critical temperature T_c (up to $\approx$ 17 K, depending on film thickness) and thus large energy gap, limiting the useful spectral range to near-infrared and higher-energy photons. In the search for alternatives we have focused on TaN, which is chemically and structurally very similar to NbN. We have started our investigations by preparing a series of TaN thin films in a multi-purpose DC-magnetron sputtering machine (FIRST Lab, ETH Zürich). The films were then dry-etched by reactive-ion etching to form standard 4-point bridges for resistivity measurements. By adjusting the sputtering conditions we could easily vary the nitrogen content in the resulting films and achieve critical temperatures of about $T_c \approx 8$ K for a ≈ 27 nm thick film. Further parameters obtained from an analysis of magneto-conductivity measurements are listed in Tab. 13.1 and are compared to those of NbN [1].

Tab. 13.1 – Some important material parameters of TaN thin films in comparison with NbN. λ is the magnetic penetration depth and N_0 is the electron density of states at the Fermi-energy. Other parameters are explained in the text.

	T_c (K)	$\xi(0)$ (nm)	$\lambda(0)$ (nm)	D (cm^2/s)	N_0 (10^{47} m^{-3}J^{-1})
TaN	8	5.0	700	0.5	2.0
NbN	16	4.5	400	0.5	3.5

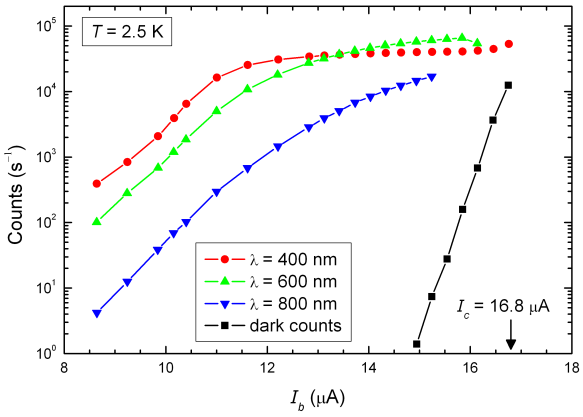

Fig. 13.1 – Count rates of a TaN SNPD measured at 2.5 K as a function of the applied bias current for three different photon wavelengths as indicated in the graph. The dark and background counts are also plotted for comparison. The appearance of a plateau of nearly constant count rates for 400 and 600 nm photons is indicative of absorption-limited detection efficiency.

Our collaborators at the Karlsruhe Institute of Technology were able to further improve the quality of TaN thin film structures in a dedicated sputtering setup. They have now reached critical temperatures up to $T_c \approx 10$ K for relatively thick films, which decreases to ≈ 8 K in films as thin as 3 nm. Very recently we were able to characterize a meander structure of dimensions typical for SNPD. A preliminary analysis of the results shows that it is possible to fabricate successfully operating detectors (see Fig. 13.1). They appear to be stable over extended periods of time with no degradation and can be easily operated over a large range of operating conditions. An extended analysis and comparison to NbN SNPD is under way.

Our interest in TaN as a detector material has been motivated also by a second focus. Although research in SNPD over roughly the last ten years has mainly been aimed at their performance as detectors for visible and near-infrared photons, essentially the same detection mechanism has already been proposed long before for higher energy keV X-ray photons [2] or even for detecting MeV alpha-particles [3]. To be able to test the detector properties for X-ray photons, we have designed and installed a setup with a *NEPTUNE* 50 kV X-ray source from *OXFORD Industries* (see Fig. 13.2), including adequate radiation shielding and, together with the Electronics Workshop, the necessary control electronics for safe operation.

The setup was tested at the end of 2010 with a conventional NbN SNPD that was optimized for optical photons. In Fig. 13.3 we show 20 traces of X-ray absorption events recorded with a digi-

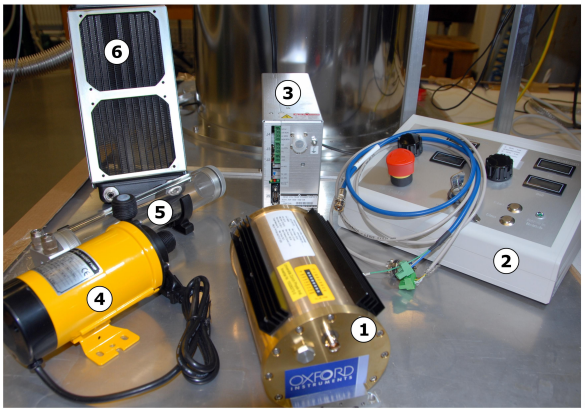

Fig. 13.2 – Parts of the X-ray source setup: 1 X-ray source, 2 control electronics (made in-house), 3 high-voltage supply, 4 water pump, 5 water reservoir, 6 radiator.

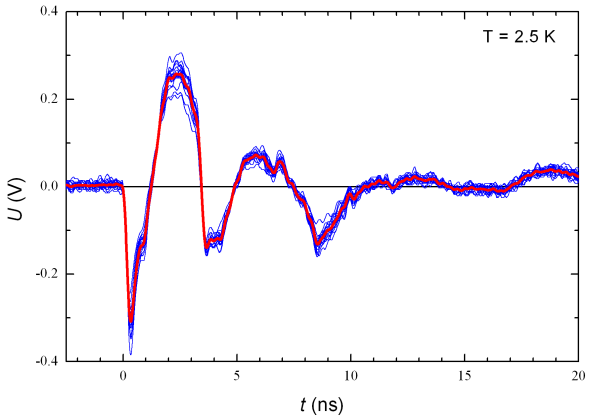

Fig. 13.3 – Traces of 20 recorded pulses after X-ray photon absorption (blue lines) and the average pulse shape (red line).

tal oscilloscope (blue lines) and the average pulse shape of these 20 pulses (red line) demonstrating its functionality. Based on the absorption probability for keV-X-ray photons in nanometer-thin NbN films we have to assume, however, that most of the photons were not absorbed in the superconducting structure, but rather in the sapphire substrate. The corresponding absorption events were thus probably triggered by secondary excitations, *e.g.* phonons or secondary electrons. This fact will have a detrimental effect on the very small jitter of the detector, one of the great advantages of SNPD compared to other single-photon detectors, because the timing of the detection event will depend on the absorption depth inside the substrate.

Therefore, TaN may be the detector material of choice since its absorption length for keV-photons is up to by a factor of 10 shorter than that of NbN. Already 100 nm thick TaN films should have an absorption probability of several percent, which might be sufficient for certain applications. On the other hand, such relatively thick films involve a number of new challenges, particularly for the nanofabrication process. We have adapted our process steps accordingly and we are now able to produce high-quality structures of the required dimensions. Our next goal will be to test X-ray SNPD based on $\sim$ 100 nm thick films.

13.2 First-order phase transition deep in the vortex state of $YBa_2Cu_3O_7$

Small-angle neutron-diffraction experiments (SANS) on the vortex lattice in clean, detwinned and fully oxygenated $YBa_2Cu_3O_7$ single crystals have recently revealed a previously unknown structural phase transitions within the vortex-solid phase . At $T = 2$ K and with the magnetic field directed parallel to the c-axis, its structure changes at $B \approx 2$ T from a low-field hexagonal to a distorted hexagonal phase, and at $B \approx 6.7$ T to a rhombic structure. Based on the observation of the abrupt and discontinuous changes in the lattice structure, these transitions have been suggested to

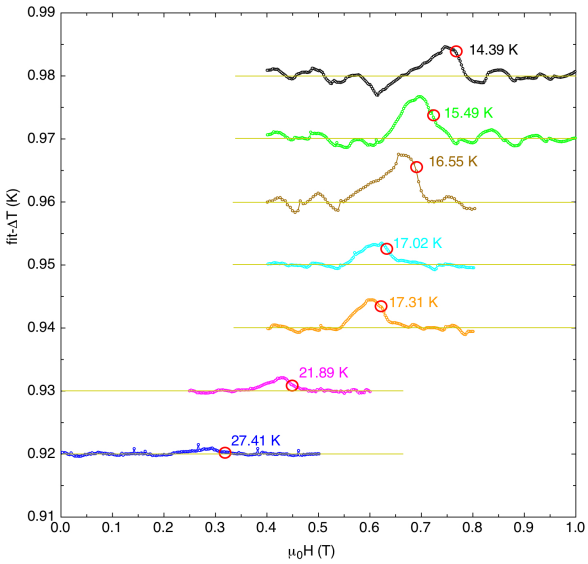

Fig. 13.4 – Magnetocaloric effect measured on a $YBa_2Cu_3O_7$ single crystal on ramping the field $\| c$ down. A polynomial background was subtracted and the curves are vertically shifted for clarity.

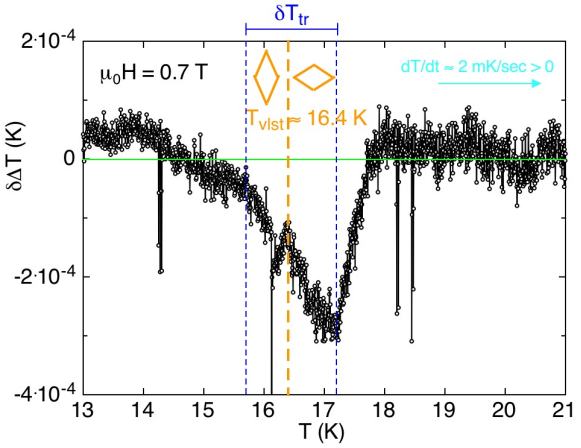

Fig. 13.5 – Temperature DTA scan showing the cooling effect due to the latent heat absorbed at the first-order phase transition.

be of first order [5].

We have investigated the magnetic phase diagram of one of the $YBa_2Cu_3O_7$ single crystals used in the above mentioned SANS study in our a home-built differential-calorimetry (DTA) setup and in a commercial SQUID magnetometer. In Fig. 13.4 we show the magnetocaloric effect, *i.e.*, the change of the sample temperature on varying the magnetic field, measured with a superimposed longitudinal a.c. magnetic field with an amplitude $\mu_0 h_{ac} \approx$

0.4 mT at a frequency $f = 11$ mHz. On entering the low-field phase from the high-field phase, the sample temperature rises by certain amount before relaxing again to the base temperature of the experiment. In a related experiment in a constant magnetic field but with increasing temperature we observed a corresponding cooling-effect when crossing the phase-transition line from below (Fig. 13.5). The measured variations in sample temperature are therefore indeed related to abrupt changes in entropy of the sample and cannot simply caused by dissipative thermal effects induced by a possible vortex motion that would lead to a heating effect in all cases. Knowing the thermal constants of the experiment, these variations in temperature can be converted to changes in entropy ΔS that we show in an inset of Fig. 13.6 [6].

A further very strong evidence that the observed thermal effects are stemming from a true thermodynamic first-order phase transition comes from corresponding magnetization M measurements, in which we observed step-like features ΔM (not shown here) than can be related to ΔS using the Clausius-Clapeyron relation. The resulting estimated changes in entropy agree reasonably well with the corresponding thermal data (see inset of Fig. 13.6), and we therefore conclude that we have found a thermodynamic evidence for a true first-order phase transition in the vortex state of $YBa_2Cu_3O_7$.

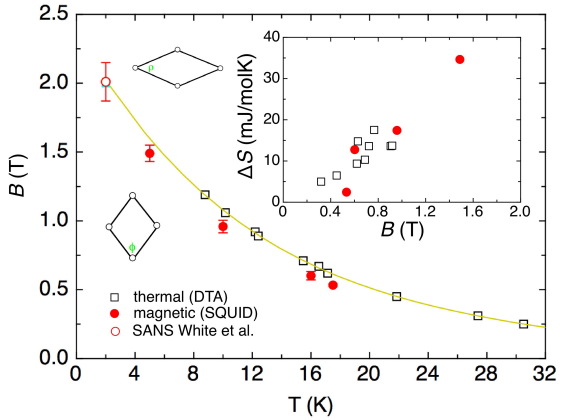

Fig. 13.6 – Phase diagram and entropy difference of a detwinned $YBa_2Cu_3O_7$ single crystal between the high-field and the low-field phase as derived from thermal DTA and SQUID magnetometry data.

13.3 A.c.-calorimetry set up for vortex-shaking experiments

In the last annual report we have announced an a.c. calorimetry set up with a resistive thermometer. The main improvements in the thermal design as compared to our previous set up are a significant reduction of the heat capacity of the sample platform and a replacement of the heat link by an adjustable link consisting of a thin copper wire. This approach has the advantage that the same sample platform can be used over a wide range of temperatures with an appropriate choice of the heat link. The sample temperature is now measured with a resistive thermometer (bare Cernox 1050 chip) in a Wheatstone-bridge configuration. The measuring frequencies in typical a.c.-calorimetry experiments are of the order of 1 Hz or below and are dictated by the sample heat capacity and the thermal conductivity of the used heat link [7]. To reduce both electrical interference and the $1/f$ noise in the fairly noisy environment of the PPMS (*Physical Property Measurement System, Quantum Design Inc.*), the small amplitude of the low-frequency temperature oscillations is measured as follows: we excite the sample thermometer with a carrier frequency of 45 kHz that is modulated with the low-frequency measuring signal. The reference resistor in the Wheatstone bridge is computer controlled and can be automatically adjusted to minimize the measured voltage difference and therefore also to maximize the measuring range of the used lock-in amplifier. The amplitude of the low-frequency component of the signal (typically measured during $\approx$ 100 sec) is finally obtained by fast-Fourier transformation of the output signal of the lock-in amplifier. In this way, both the $1/f$ noise and other sources of electrical noise are dramatically reduced [8]. With the result of this procedure and the known values for excitation current, frequency and reference resistors we can calculate the resulting amplitude of the low-frequency oscillation in the temperature of the sample platform. This can finally be used to obtain the heat capacity of the sample platform carrying the sample of interest.

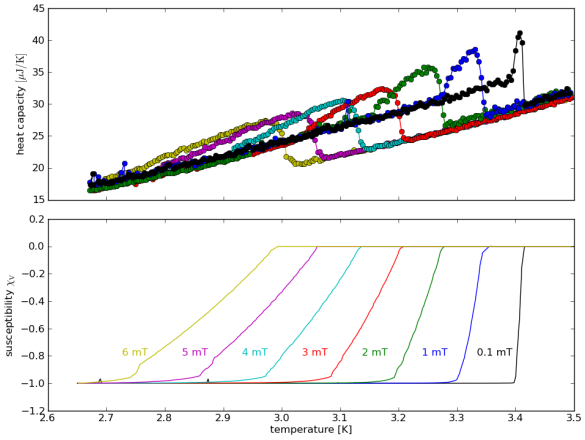

Fig. 13.7 – Upper part: Test measurement of the specific heat of a 37 mg In sample on a sample platform in an external magnetic field, measured with the here described home built a.c. calorimetry experiment. Lower part: Real part of the a.c. susceptibility of the same sample (see text).

In Fig. 13.7 we show the result of a corresponding test measurement, taken at the transition form the normal to the superconducting state of an indium sample (37 mg) in various magnetic fields and with an amplitude $\approx$ 1 mK of the temperature oscillation. As indium is a type-I superconductor, the transition to superconductivity in a finite magnetic field is of first order (see related peaks in the heat capacity in Fig. 13.7). Moreover, depending on the sample geometry, the sample enters an inhomogeneous intermediate state upon cooling below the transition temperature, which results in a broadening of the transition as measured both by a.c. susceptibility and specific heat (upper and lower part of Fig. 13.7).

This kind of test measurement confirms that we have achieved a sufficient accuracy for our purpose (detecting first order and continuous phase transitions) with a very low instrumental broadening on the temperature scale ($\approx$ 1 mK). It is worth mentioning that the present design also allows for measurements of the magnetocaloric effect or for conventional continuous-heating and relaxation experiments to measure heat capacities, respectively, with or without the application of an external "shaking" a.c. magnetic field.

13.4 Possible lattice distortion at the Bose-Einstein condensation of magnetic bosonic quasiparticles in $TlCuCl_3$

We have suggested that the positions of the spin-carrying atoms in certain magnetic insulators might discontinuously change at the critical field H_c (*i.e.*, at the onset of antiferromagnetic ordering), in some resemblance to a Spin-Peierls instability in one dimensional magnetic chains [9]. We stated that a thorough structural analysis around this magnetic phase transition of any magnetic insulator is indispensable. We have therefore done corresponding experiments on single crystals of $TlCuCl_3$ (provided by Dr. Karl Krämer, University of Bern), using neutron diffraction and X-ray diffraction methods in order to increase the significance of our experiments.

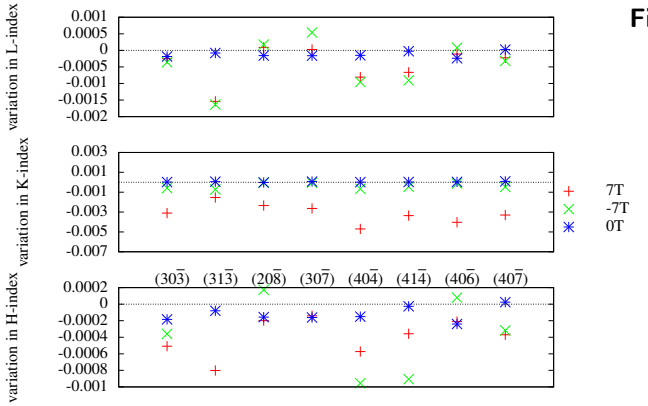

Fig. 13.8 – Variation of selected X-ray peak positions in applied magnetic fields of $\mu_0 H = 0$ T, 7 T and -7 T, as compared to a first measurement without magnetic field. The shown variation of the peak indices (HKL) is measured with respect to the reciprocal lattice units of the original zero-field measurement based on the unit cell given in [10]. The peaks are labeled in the lower panel and ordered according to their scattering angle. The equal spacing on the x-axis was chosen to increase clarity of the plot and does not reflect the value of the scattering angle.

The X-ray measurements were performed at the ID20-beamline of the ESRF in Grenoble. In order to detect a change in crystal symmetry, eleven peaks were selected, including peaks forbidden by the P 21/c symmetry of $TlCuCl_3$ in the normal (*i.e.*, unmagnetic) phase. The chosen peaks were studied using a wavelength of $\lambda = 1.4$ Å ($E = 8.9$ keV), near the copper K-edge) at $T = 2.5$ K and applied fields of $\mu_0 H = 0$ T, 7 T and -7 T to eliminate possible magneto-elastic effects of the experimental offset.

We observed apparently field-induced shifts of certain peak positions (see Fig. 13.8). However, we were not yet able to develop a scenario that consistently reproduces all the measured data. Therefore we cannot draw a final conclusion about a possible structural change at the transition to the antiferromagnetic state based on these data alone.

The neutron-diffraction experiments were performed at the RITA-II spectrometer at the PSI in Villigen. The peaks were investigated at $T = 2$ K with several different magnetic fields in a range between $\mu_0 H = 0$ to 13.5 T since it was not possible to identify a clear trend in peak position and intensity based on only two magnetic fields used in the X-ray experiments.

The relative development of the position, height and width of the peaks does not show a common trend nor any abrupt change of relevant magnitude at the critical field $\mu_0 H \approx 6$ T. In Fig. 13.9 we plotted the variation of the corresponding intensities as a function of magnetic field. The change of the lattice parameters was estimated from the change of the peak positions, and the resulting changes in the peak intensity were simulated based on this result. This simulated variation of the peak intensity was by almost one order of magnitude larger than the experimental variation of the peak height, however, which clearly shows that the true change of the peak position must be much smaller than the experimental resolution achieved in this experiment.

To conclude, the proposed sizeable distortion of the crystal symmetry could not be confirmed for $TlCuCl_3$ up to now.

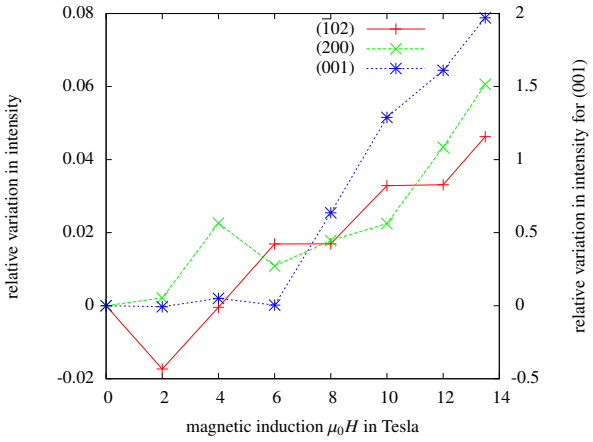

Fig. 13.9 – Relative variation of the neutron peak intensity I. Plotted is the relative difference $(I(0) - I(H))/I(0)$ where $I(0)$ is the measurement for $H = 0$. Note that for the (001)-Peak the right scale applies. The lines are guides to the eye.

[1] H. Bartolf, doctoral thesis, University of Zürich, 2009.

[2] A. Gabutti *et al.*, Nucl. Instrum. Methods A, **278**, (1989) 425.

[3] D. E. Spiel *et al.*, Appl. Phys. Lett., **7**, (1965) 292.

[4] A. J. Kerman *et al.*, Phys. Rev. B, **79**, (2009) 100 509(R).

[5] J. S. White *et al.*, Phys. Rev. Lett., **102**, (2009) 097001.

[6] A. Schilling and M. Reibelt, Rev. Sci. Instrum., **78**, (2007) 033904.

[7] O. M. Corbino, Phys. Zeits., **11**, (1910) 413.

[8] J. H. Scofield, Am. J. Phys., **62**, (1994) 129.

[9] R. Dell'Amore *et al.*, Phys. Rev. B, **79** (2009) 014438.

[10] H. Tanaka *et al.*, J. Phys. Soc. Jpn., **70**, (2001) 939.